Behavior of Alumina-Magnesia Complex Inclusions and Magnesia Inclusions on the Surface of Molten Low-Carbon Steels

SEI KIMURA, K. NAKAJIMA, and S. MIZOGUCHI

It is well known that alumina inclusions on the surface of molten Al-killed steel quickly attract each other to form clusters. On the other hand, alumina-magnesia complex inclusions on the surface of molten low-carbon steel with a high oxygen content have a much weaker tendency to form clusters. In the present work, the reason for the different behaviors of the two types of inclusions was analyzed in detail. A confocal scanning laser microscope was used to carry out the experiment of *in-situ* observation of the two types of inclusion on the molten pool. The first type of inclusion was 93 mass pct alumina-7 mass pct magnesian, obtained in a Mg-added Al-killed steel. The second type of inclusion was nearly pure magnesia, obtained in a Mg-killed steel. The attractive force between a pair of inclusions, for both cases, was found to be approximately $1O^{-17}$ to 10^{-16} N and one-tenth of that between a pair of alumina inclusions. The various effects of contact angle, surface tension, and oxygen content of the steel melt on the attractive force are discussed in detail from the viewpoint of the capillary force.

I. INTRODUCTION

AMONG various types of nonmetallic inclusions, oxide and sulfide inclusions have been thought harmful for common steels. However, there are some positive roles for these inclusions. Oxide inclusions act as the trapping sites of hydrogen atoms in enameled steel and prevent the coating film from stripping off. Sulfide inclusions also improve the machinability of free-cutting steels. Furthermore, it has been well known in welding that the tiny oxide inclusions act as the nucleation sites for very fine acicular ferrite crystals in the bond metal, giving a very good ductility.[1–5] In the rolled steel products too, many fine intragranular ferrite crystals nucleate at some oxide inclusions inside of austenite grains. This technique is based on the concept of oxides metallurgy,[6] in which an important role is given to oxide inclusions as inoculants for the heterogeneous nucleation of the phase transformation and the precipitation. It has certainly been known in principle that the heterogeneous nucleation gives rise to the grain refinement, and that the precipitation often occurs at the nucleation sites of inclusions. However, in the concept of oxide metallurgy, the the oxide particles are intentionally controlled, from the beginning of the steelmaking process, for the subsequent nucleation. This concept is new, particularly from the viewpoint of the new overall processing of the heterogeneous nucleation, combining the steelmaking process with the following heat-treatment and rolling processes.

In order to make oxide inclusions useful for this purpose, the composition, size, and distribution must be controlled properly. For example, alumina inclusions appearing in the normal aluminum-killed steel have a strong attractive force between them and show a remarkable tendency to coagulate and to form clusters.[7] Alumina inclusions also show a weak capability for MnS to precipitate on alumina inclusions.[8] In view of such behavior, alumina inclusions seem not to be interesting.

On the other hand, alumina-magnesia complex inclusions have a much weaker tendency to coagulate and to form clusters than alumina inclusions.[9] In this study, the attractive force between a pair of inclusions such as alumina-magnesia complex inclusions and magnesia inclusions is measured by using a confocal scanning laser microscope. The reason why the behavior of these inclusions is entirely different from that of alumina inclusions will be explained further, in detail, through morphological analysis and theoretical calculations.

II. EXPERIMENTS

A. *Specimen*

Two samples were used. Sample A is a Mg-added Al-killed steel with a high oxygen content. A 100 g portion of a low-carbon aluminun-killed steel was cut out from a continuously cast slab and remelted under Ar gas flow in an alumina crucible in a 5 kW electric resistance furnace. Subsequently, the 5 g Fe-10 mass pct Mg pressed-powder cake was added to the molten steel. When Mg metal was added to the melt, a strong boiling took place and the melt absorbed oxygen from the ambient air entering from the top port. The melt was cooled in the furnace by switching off the power, and sample A, with a high total oxygen content was, thus, obtained. Sample B is low-carbon Mg-killed steel with a low oxgen content. The vacuum arc furnace was used to prevent the sample from oxygen absorption. Quantities of 100 g of electrolytic iron, 0.5 g of an Fe–70 mass pct Mn alloy, 0.05 g of an Fe–20 mass pct S alloy, and 0.1 g carbon were mixed and remelted in a vacuum arc furnace, and the mother alloy was made. It was then remelted again in the vacuum arc furnace, and 3 g Fe–10 mass pct Mg

SEI KIMURA, Research Fellow dispatched from Kakogawa Works, is with Kobe Steel Co. Ltd., Kakogawa 675-0023, Japan. K. NAKAJIMA, Associate Professor, and S. MIZOGUCHI, Professsor, are with the Institute for Advanced Materials Processing,Tohoku University, Sendai 980-8577, Japan

Manuscript submitted April 3, 2000.

Table I. Chemical Composition of the Specimens

Sample	C	Si	Mn	P	S	Al	Mg	Total O
A (before)	0.04	<0.01	0.02	0.006	0.006	0.002	<0.0001	0.1314
A (after)								0.0581
B (before)	0.04	<0.01	0.21	<0.004	0.012	<0.001	0.0005	0.0008
B (after)								0.0013

pressed-powder cake was added to the melt of the mother alloy for the complete deoxidization. Sample B, with a low total oxygen content, was, thus, obtained. The chemical analyses were made twice for both samples, before and after the *in-situ* observation experiment, in order to confirm the total oxygen content. Table I shows the results of the chemical analysis. The reason for the change in oxygen content before *vs* after the *in-situ* observation is the removal of the oxide inclusions from the melt to the surface. But the sample was not completely melted, nor did the oxide inclusions completely float up to the surface. The inclusions always existed during the observation. It is conceivable that oxide inclusions are observed under total oxygen contents above 600 ppm. This value is still large enough for the observation of the effect of oxygen on the characteristic inclusion behavior. Therefore, it may be concluded that the stable phenomena were observed.

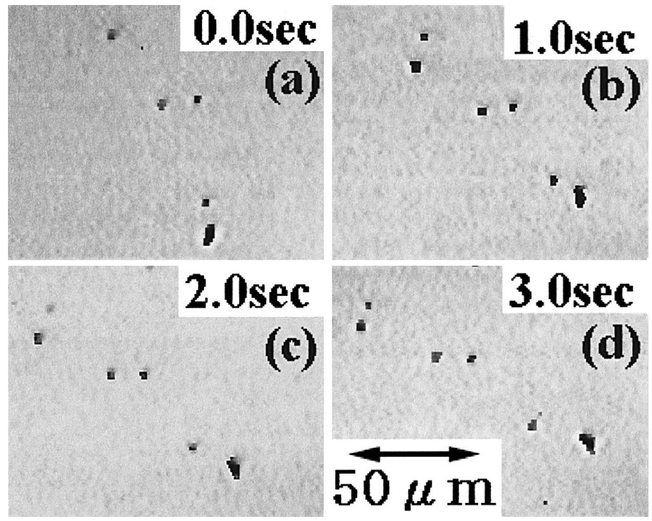

Fig. 1—(*a*) through (*d*) Typical examples of alumina-magnesia complex inclusions showing no interaction (sample A).

B. *In-situ Observation*

A confocal scanning laser microscope was used for the *in-situ* observation of inclusions on the molten steel surface. The principle and the method of operation of the laser microscope have been described in detail elsewhere.[7,9,10] A small piece of each sample was machined into a disc (4.3 mm in diameter and 2 mm in height), mirror polished, and melted in an alumina crucible (5.5 mm o.d. and 4.5 mm i.d.) under ultrahigh-purity Ar gas. The temperature was measured at the bottom of the holder of the crucible. The power was controlled to always keep the temperature near the liquidus. Special attention was paid not to melt the sample completely, but to leave a thin solid shell of steel at the periphery of the crucible. This solid shell prevented nonmetallic inclusions existing in the melt from being absorbed into the crucible. The movement of inclusions on the molten surface was observed at magnifications of up to 2100 times, with a resolution of 0.5 μm. The images were monitored on a cathode-ray-tube monitor and recorded on videotape at intervals of 1/30 of a second. The position of each small particle was traced on the video pictures at each interval. Thus, the velocity and the acceleration of the particles could be measured as a function of the distance between the two particles. The force between the two particles was then calculated by Newton's equation, assuming a spherical shape. After the observation, the sample was gas quenched in the microscope. The shape and the chemical composition of the inclusions on the quenched sample were analyzed by electron-probe microanalysis (EPMA), scanning electron microscopy (SEM), and auger electron spectroscopy (AES).

III. RESULTS

A. *Characteristics of Alumina-Magnesia Complex Inclusions (Sample B) and Magnesia Inclusions (Sample B)*

Yin *et al.*[10] showed that a strong long-range attraction exists among alumina inclusions on low-carbon aluminum-killed steel melts. On the contrary, alumina-magnesia inclusions and magnesia inclusions behave in entirely different manners. Figures 1 and 2 show typical examples of alumina-magnesia inclusions and magnesia inclusions, respectively. Tiny particles uniformly disperse on the molten pool and stay quietly, exhibiting a very weak coagulating or clustering tendency. Figure 3 is the overlooking view and Figure 4 is the cross-sectional view of the alumina-magnesia complex inclusions, with the higher-magnification image left on the surface of the quenched sample A. The composition of these particles was analyzed by EPMA and found to be 93 pct alumina-7 pct magnesia in mass.

Furthermore, SEM and AES were used to investigate these alumina-magnesia inclusions in detail. Figure 5 is a microscopic image by SEM of one particle of an alumina-magnesia inclusion. It is very interesting that the particle consists of a core and a periphery crystal. Figure 6 shows auger spectra of some element (a) in the core and (b) in the periphery. Aluminum and oxygen are detected both in the core and in the periphery. Surprisingly, magnesium could be detected only slightly in the core, but not in the periphery.

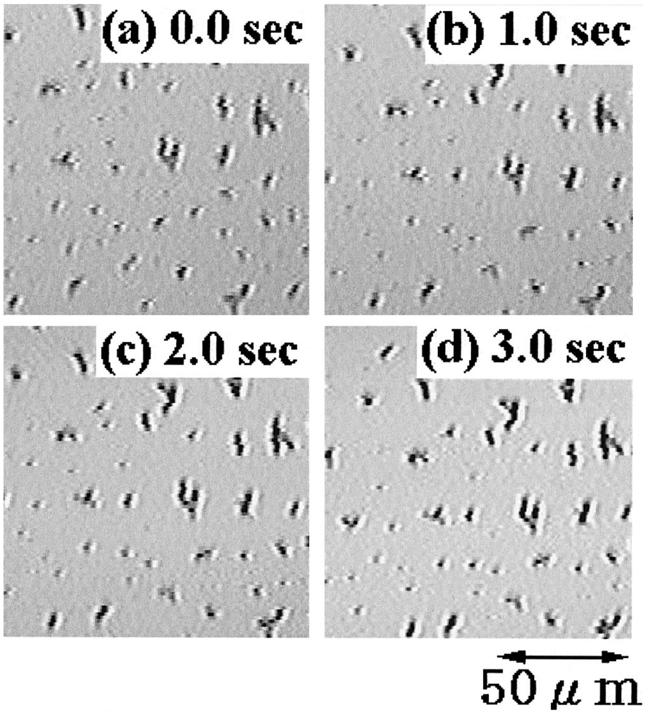

Fig. 2—(*a*) through (*d*) examples of magnesia inclusions showing no interaction (sample B).

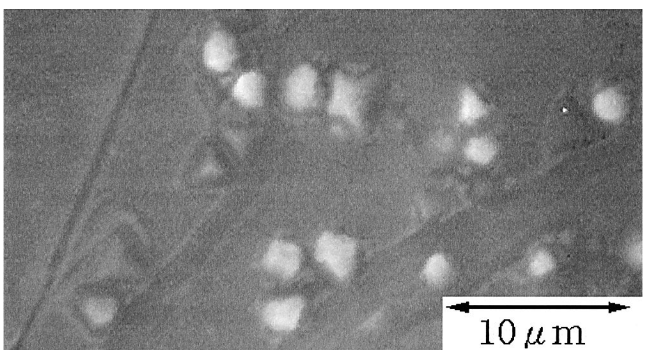

Fig. 3—Particles of alumina-magnesia complex inclusions after quenching (sample A).

B. *Attractive Force between a Pair of Inclusions*

An evaluation of the attractive force was carried out based on the measurement of acceleration and the estimation of the mass of inclusions, as shown in Figure 7. The inclusion shape was assumed to be a disc. The change in the distance of two inclusions was measured from d_1 to d_3. A thickness of 2 μm was determined, based on the observation at the cross section of an inclusion, as shown in Figure 4. The radii of each disc (R^*_1 and R^*_2) were measured also on the figures of *in-situ* observation of inclusions on the steel melt surface. The terms R^*_1 and R^*_2 were taken to be the geometric average of $R^*_1 = (C_{11} \cdot C_{12})^{0.5}/2$ and $R^*_2 = (C_{21} \cdot C_{22})^{0.5}/2$. The acceleration ($A_1$) of the guest inclusion was determined from the change in the position of the guest inclusion at Δt (equal to 1/30 of a second) intervals when the host inclusion in the pair stayed quiescent. The attractive force (F_{abs}) was given by Eqs. [1] through [5].

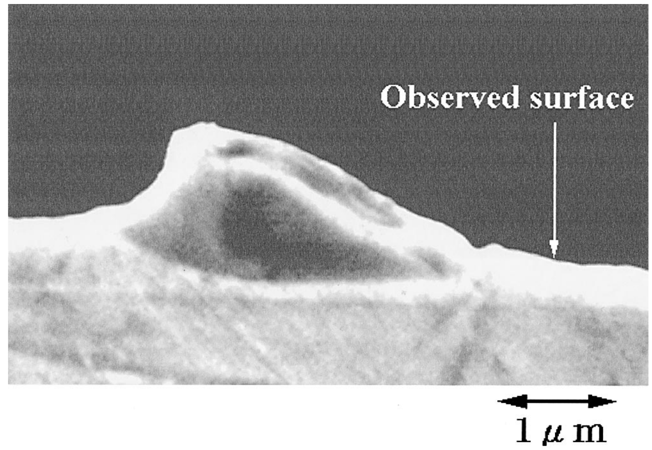

Fig. 4—Micrograph of the cross section of a complex inclusion (sample A).

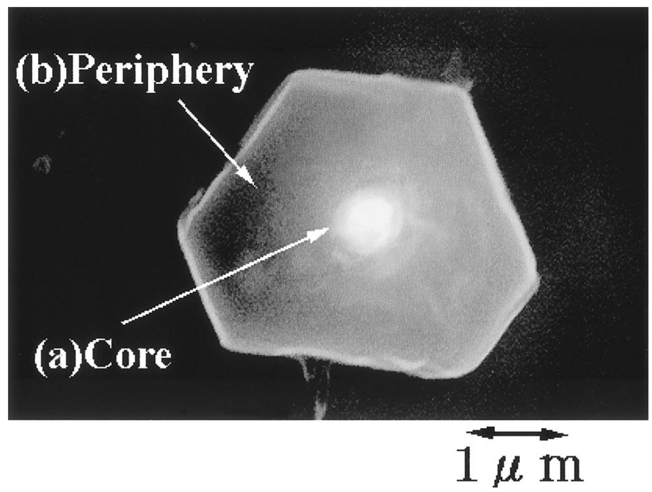

Fig. 5—SEM micrograph of one particle of alumina-magnesia complex inclusions (sample A).

$$V_1 = (d_2 - d_1)/\Delta t \qquad [1]$$

$$V_2 = (d_3 - d_2)/\Delta t \qquad [2]$$

$$A_1 = (V_1 - V_2)/\Delta t \qquad [3]$$

$$m_1 = 2\pi R^*_1 \cdot R^*_1\, w \times \rho_P \qquad [4]$$

$$F_{obs} = m_1 \cdot A_1 \qquad [5]$$

where d_1, d_2, and d_3 are the distances between the two particles at 1/30, 2/30, and 3/30 of a second before the collision, respectively; V_1 and V_2 are the average velocities of the guest inclusion from 1/30 to 2/30 of a second and from 2/30 to 3/30 of a second before the collision, respectively; m_1 is the mass of the guest inclusion; and ρ_P is the density of the inclusions. The observed distance between the two particles at 2/30 of a second before collision, that is, d_2, was defined as the acting length. Furthermore, the maximum acting length was defined as the greatest value of these observed lengths. These terms are defined similarly to Yin's definition[7] in order to compare the present results with his results. The observed distance between the two particles at 2/30 of a second before collision, that is, d_2, was defined

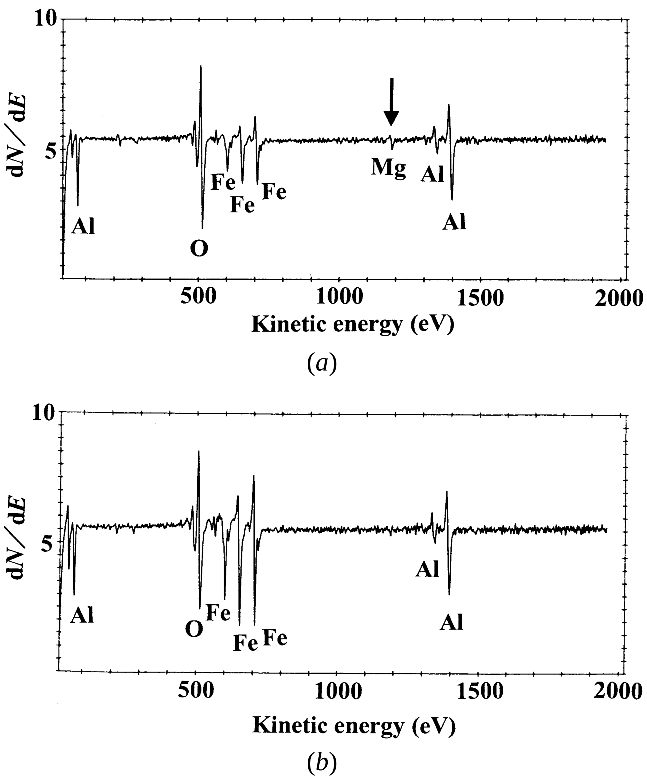

Fig. 6—Auger spectra of elements (*a*) in the core and (*b*) in the periphery.

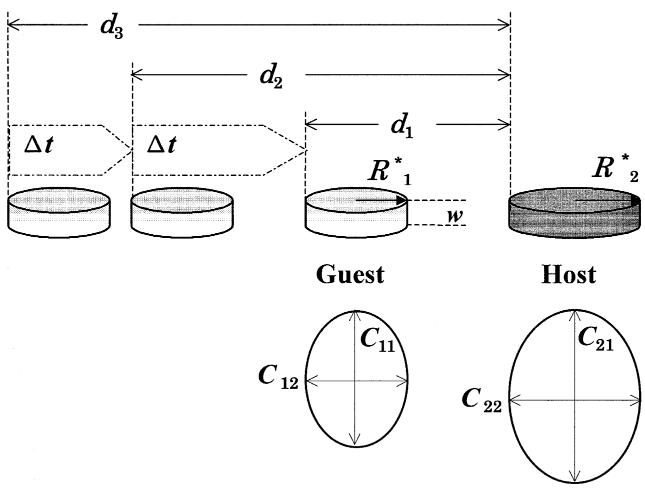

Fig. 7—Schematic illustration to derive attractive force from the observed change in the position of inclusions in pair.

as the acting length. Furthermore, the maximum acting length was defined as the greatest value of these observed lengths. These terms are defined similarly to Yin's definition, in order to compare the present results with his results. If two inclusions moved simultaneously, a revision was made by substituting $m_1 \cdot m_2/(m_1 + m_2)$ for m_1 in Eq. [5], where m_2 is the mass of the larger inclusions

The derived attractive forces between a pair of alumina-magnesia complex inclusions and between a pair of magnesia inclusions are shown in Figure 8 as a function of the acting length. The attractive forces derived by Yin *et al.*[7,10] between a pair of alumina inclusions and between a pair of

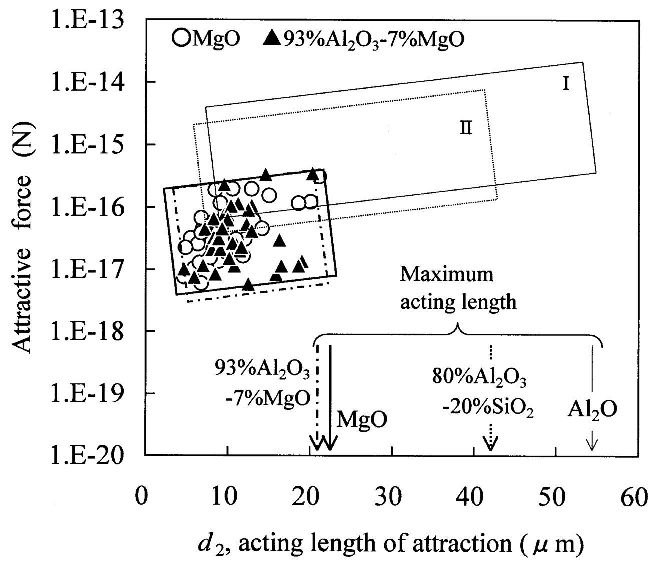

Fig. 8—Attractive forces measured between alumina-magnesia complex inclusions in pair and between magnesia inclusions in pair: (I) Al_2O_3 and (II) 80 pct Al_2O_3-20 pct SiO_2 by Yin *et al.*[7]

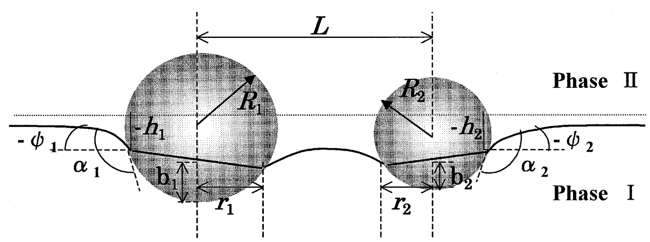

Fig. 9—Schematic illustration of the capillary meniscus around two spherical particles.

80 mass pct alumina-20 mass pct silica inclusions are also shown in the same figure. The force obtained in the present work between alumina-magnesia complex inclusions is in the range from 5×10^{-18} to 5×10^{-16} N, and it is approximately the same as the force between the magnesia inclusions. The forces between these two kinds of inclusions are approximately 1/10 of the force between the alumina inclusions. The maximum acting lengths for alumina-magnesia complex inclusions and magnesia inclusions are 21 and 22 μm, respectively. These values are about two-fifths of, and much shorter than, the maximum acting length for alumina inclusions. Alumina-magnesia complex inclusions and magnesia inclusions coagulate only when the distance between the two particles becomes smaller than that for alumina inclusions. That is, they are more difficult to coagulate than alumina inclusions.

IV. DISCUSSION

When two solid spherical particles exist at the interface of the two phases, the meniscus of the interface around the particle will be deformed by a capillary effect to create an interaction between the two particles. Kralchevsky *et al.*[11] have generally derived the mathematical equations for the energy and force balance between two particles floating on the surface of liquid. Then, Paunov *et al.*[12] considered a simplified situation, as shown in Figure 9, and proposed a procedure to calculate the energy and the force of the capillary interaction between the two floating spherical particles existing at the gas-liquid interface, based on the general expression of the thermodynamic potential. In the present analysis, the shape of the inclusion was assumed to be a disc, so as to compare the attractive forces derived from the present results with those of the alumina and alumina-silicate inclusions shown in Yin's report.[7] Paunov's theory[11,12] originally dealt with spherical particles, but it was applied to particles of a disc shape simply because the mathematical analysis on the disc was too complicated. Nevertheless, the application of Paunov's theory is considered to be very useful in this case for the semiquantitative evaluation of the order of magnitude of the attractive force.

They have theoretically derived an equation for the capillary interaction energy between the two spherical particles 1 and 2, as follows:

$$\Delta W = -\pi\gamma \sum_{k=1}^{2} (Q_k h_k - Q_{k\infty} h_{k\infty})(1 + O(q^2 R_k^2)) \quad [6]$$

where the subscript k represents particles 1 and 2, ∞ means that the distance between the two particles is infinite, q is defined as $1/(\gamma/(\rho_{\mathrm{I}} - \rho_{\mathrm{II}})g)^{1/2}$, and $O(y)$ is the zero-order function of approximation. The value of Q_k and the height difference (h_k) at the distance of L can be derived, respectively, by

$$Q_k = \frac{1}{2} q^2 \left(b_k^2 \left(R_k - \frac{1}{3} b_k \right) - \frac{4}{3} D_k R_k^3 - r_k^3 h_k \right) \quad [7]$$

and

$$h_k = Q_k(\tau_k + 2 \ln(1 - \exp(-2\tau_k))) - (Q_1 + Q_2) \ln(\gamma_e q a) + (Q_1 - Q_2)\left(A - (-1)^k \sum_{n=1}^{\infty} \frac{2}{n} \frac{\exp(-n\tau_k) \sinh n\tau_j}{\sinh n(\tau_1 + \tau_2)} \right),$$

$$j \text{ and } k = 1 \text{ and } 2, j \neq k; (qR_k)^2 \ll 1 \quad [8]$$

where $\gamma_e = 1.78$ (ln γ_e being the constant of Euler–Masceroni) and

$$A = \sum_{n=1}^{\infty} \frac{1}{n} \frac{\sinh n(\tau_1 - \tau_2)}{\sinh n(\tau_1 + \tau_2)} \quad [9]$$

$$\tau_k = \ln(a/r_k + (a^2/r^2 + 1)^{0.5}) \quad [10]$$

$$a^2 = (L^2 - (r_1 + r_2)^2)(L^2 - (r_1 - r_2)^2)/(2L)^2 \quad [11]$$

$$D_k = (\rho_k - \rho_{\mathrm{II}})/(\rho_{\mathrm{I}} - \rho_{\mathrm{II}}) \quad [12]$$

$$b_k = R_k (1 + \cos(\alpha_k + \psi_k)) \quad [13]$$

$$\psi_k = \arcsin(Q_k/r_k) \quad [14]$$

$$r_k = 0.5 (R_k \sin \alpha_k + (R_k^2 \sin^2 \alpha_k + 4 Q_k R_k \cos \alpha_k)^{1/2} \quad [15]$$

When L approaches ∞, $Q_{i\infty}$ and $h_{i\infty}$ become

$$Q_{k\infty} = \frac{1}{6} q^2 R_k^3 (2 - 4D_k + 3 \cos \alpha_k - \cos^3 \alpha_k) \quad [16]$$

and

$$h_{k\infty} = r_{k\infty} \sin \alpha_k \psi_{k\infty} \frac{4}{\gamma_e q r_{k\infty}(1 + \cos \psi_{k\infty})} \quad [17]$$

Once ΔW is calculated at the different values of L, the capillary interaction force (F) is given by the following equation:

$$F = d(\Delta W)/dL \quad [18]$$

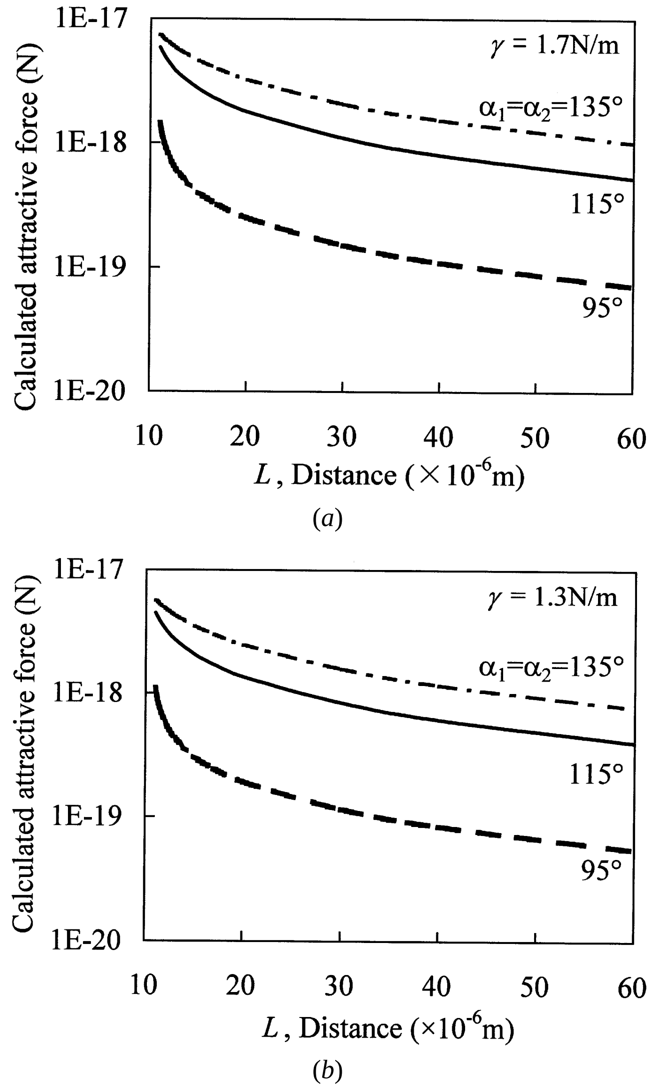

Fig. 10—Relationship between calculated attractive force and acting length in the case of (a) $\gamma = 1.7$ N/m; (b) $\gamma = 1.3$ N/m, using $\rho = 7000$ kg/m^3; and $\rho_1 = \rho_2 = 4000$ kg/m^3, $R_1 = R_2 = 5.3 \times 10^{-6}$ m.

Figure 10 shows the results of the calculation of F *vs* L. This figure shows that the attractive force becomes larger as two particles of a fixed size approach each other. Here, it must be reiterated that Figure 8 shows a different relationship between the attractive force and d_2, the acting length. This figure shows that a larger attractive force is needed when the acting length is large. Figure 10(a) corresponds to low-oxygen steel ($\gamma = 1.7$ N/m), and Figure 10(b) corresponds to high-oxygen steel ($\gamma = 1.3$ N/m). The values of the contact angle between the inclusions and molten steel are given as $\alpha_1 = \alpha_2 = 95$, 115, and 135 deg, respectively. The values of the densities of the inclusions, molten steel, and gas are $\rho_1 = \rho_2 = 4000$ kg/m^3, $\rho_1 = 7000$ kg/m^3, and $\rho_{\mathrm{II}} = 0$, respectively. The value of the radii of inclusions is given as $R_1 = R_2 = 5.3 \times 10^{-6}$ m by considering the volume of the spheres to be the same as that of the discs, of which the radii R^*_1 and R^*_1 are 10×10^{-6} m. Comparing Figures

10(a) with (b), it is shown that the surface tension of the steel melt (γ) alone hardly affects the calculated attractive force.

On the contrary, the attractive force is rather dependent on the contact angle. For example, $F = 10^{-19}$ to 10^{-18} N when $\alpha_1 = \alpha_2 = 95$ deg, and $F = 10^{-18}$ to 10^{-17} N when $\alpha_1 = \alpha_2 = 115$ to 135 deg. Ogino *et al.*[13] measured the contact angle of an alumina and magnesia refractory attached to a steel melt. According to their values, the contact angle of magnesia is about 90 deg, much smaller than that of alumina (120 deg). Therefore, this is considered to be the major reason why magnesia inclusions have a weaker tendency to coagulate than alumina inclusions.

Comparing the previous calculation by Paunov's theory on the spheres shown in Figure 10 with the measurement on the discs in the present work, shown in Figure 8, there is a big difference. The theoretical values are much smaller than the measured ones, by two orders of magnitude. The reason for this discrepancy is not clear yet, but various factors may be responsible. If the estimation of force balance is erroneous, the calculation is also erroneous in Paunov's theory. The force balance is significantly affected by the position of the center of gravity, the mass, and the surface roughness of the solid inclusions. The shape of the liquid inclusions is perfectly spherical, but the shape of the solid inclusions in the present work is very irregular, as shown in Figures 3 and 4. The estimation of the position of the center of gravity and the mass of the actual solid inclusions is not easy, and the situation is not like that shown in Figure 9.

Nevertheless, the calculation itself is still useful for understanding the effects of important properties such as the interfacial energy and the contact angle on the attractive force.

Next, the reason why these two types of inclusions behave differently from alumina inclusions will be discussed in detail. It was already mentioned that the attractive force for the alumina-magnesia complex inclusions is just the same as that for the magnesia inclusions. However, AES analysis revealed that the periphery of the alumina-magnesia complex inclusions consisted of alumina in the periphery, as shown in Figure 6. Therefore, the contact angle at the periphery must be the same as that for pure alumina. If so, the attraction force between the alumina-magnesia complex inclusions in the pair must be the same as that between the alumina inclusions in the pair. This contradiction may be explained as the effect of the oxygen content in the molten steel on the contact angle between the inclusions and molten steel.

Nogi and Ogino[14] measured the contact angle of alumina and molten steel as a function of the oxygen concentration in the molten steel. Since the oxygen content was 0.05 to 0.1 mass pct in the case of alumina-magnesia complex inclusions in the present work, the contact angle between the inclusions and molten steel with such a high oxygen content will be 90 to 110 deg, according to their data. This value is significantly lower than that of pure alumina, and it will explain the reason why the alumina-magnesia complex inclusions have a much weaker attractive force than the alumina inclusion. The attractive force between alumina-magnesia inclusions becomes low because the contact angle is low, due to the high oxygen content in Mg-added Al-killed steel.

On the other hand, the attractive force between pure magnesia inclusions is also low, simply because the contact angle between pure magnesia inclusions is low in a Mg-killed steel in the present work. Therefore the contact angle is the key factor for the attraction of particles.

V. CONCLUSIONS

The results obtained will be summarized as follows, based on the *in-situ* observation and theoretical analysis of both the alumina-magnesia complex inclusions and magnesia inclusions.

1. Alumina-magnesia complex inclusions on the surface of molten steel with a high oxygen content had a much weaker tendency to coagulate or to form clusters.
2. These inclusions consisted of alumina in the periphery and magnesia in the core.
3. Magnesia inclusions on the surface of molten steel with a low oxygen content also had a weaker tendency to coagulate.
4. The attractive forces between a pair of these two kinds of inclusions are approximately the same (10^{-17} to 10^{-16} N) and are one-tenth of that between a pair of alumina inclusions. The maximum acting lengths for alumina-magnesia complex inclusions and magnesia inclusions are 21 and 22 μm, respectively. These values are about two-fifths of, and shorter than, that of alumina inclusions. Alumina-magnesia complex inclusions and magnesia inclusions coagulate only when the distance between the two particles becomes smaller than that for alumina inclusions. That is, they are more difficult to coagulate than alumina inclusions.
5. The attractive force is remarkably reduced when the contact angle is reduced. The increase in oxygen content in Mg-added Al-killed steel decreases the attractive force significantly due to the decrease in the contact angle. The contact angle is the common reason why the behavior of both alumina-magnesia complex inclusions and magnesia inclusions is very different from that of pure alumina inclusions.

NOMENCLATURE

d_1, d_2, d_3	distance between two discs
w	thickness of discs
R^*_1, R^*_2	radius of discs
C_{11}	length of long axis of guest disc
C_{12}	length of short axis of guest disc
C_{21}	length of long axis of host disc
C_{22}	length of short axis of host disc
m_1,m_2	mass of discs
ρ_p	density of discs
V_1	average velocity of guest disc at 1/30 to 2/30 of a second before collision
V_2	average velocity of guest disc at 2/30 to 3/30 of a second before collision
A_1	acceleration of guest disc
F_{obs}	attractive force observed
ΔW	capillary interaction energy
γ	surface tension between phase I and II
h_k	meniscus elevation at contact line
b_k	depth of immersion of particles inside phase I
r_k	radius of contact lines

g	gravity acceleration
R_k	radius of particles
γ_e	Euler–Masceroni constant
α_k	contact angle among particles, phase I and II
ψ_k	meniscus slope at contact line
ρ_k	density of particles
ρ_{I}	density of phase I
ρ_{II}	density of phase II
L	distance between two particles
F	capillary force

REFERENCES

1. O. Grong and D.K. Matrock: *Int. Met. Rev.*, 1986, vol. 31, pp. 27-48.
2. D.J. Abson: *Weld. World*, 1989, vol. 27, pp. 77-101.
3. J.M. Dowling, J.M. Corbett, and H.W. Kerr: *Metall. Trans. A*, 1986, vol. 17A, pp. 1611-23.
4. Z. Zhang and R.A. Farrar: *Mater. Sci. Technol.*, 1996, vol. 12, pp. 237-60.
5. J.M. Gregg and H.K.D.H. Bhadeshia: *Acta Mater.*, 1997, vol. 45, pp. 739-48.
6. J. Takamura and S. Mizoguchi: *Proc. 6th Int. Iron and Steel Congr.*, IISC, Nagoya, Japan, 1990, vol. 1, pp. 591-604.
7. H. Yin, H. Shibata, T. Emi, and M. Suzuki: *Iron Steel Inst. Jpn. Int.*, 1997, vol. 37, pp. 936-45.
8. Y. Ueshima, H. Yuyama, S. Mizoguchi, and H. Kajioka: *Tetsu-to-Hagané,* 1989, vol. 75, pp. 501-08.
9. S. Kimura, Y. Nabeshima, K. Nakajima, and S. Mizoguchi: *Metall. Mater. Trans. B*, 2000, vol. 31B, pp. 1013-21.
10. H. Yin, H. Shibata, T. Emi, and M. Suzuki: *Iron Steel Inst. Jpn. Int.*, 1997, vol. 37, pp. 946-55.
11. P.A. Kralchevsky, V.N. Paunov, N.D. Denkov, I.B.V. Ivanoc, and K. Nagayama: *J. Colloidal Interface Sci.*, 1993, vol. 155, pp. 420-37.
12. V.N. Paunov, P.A. Kralchevsky, N.D. Denkov, and K. Nagayama: *J. Colloidal Interface Sci.*, 1993, vol. 157, pp. 100-12.
13. K. Ogino, A. Adachi, and K. Nogi: *Tetsu-to-Hagané*, 1973, vol. 59, pp. 1237-44.
14. K. Nogi and K. Ogino: *Can. Metall. Q.*, 1983, vol. 22, pp. 19-28.